VOLUME 37 NUMBER 6
JUNE 2019

ISSN: 1002-0721
CODEN JREAE 6

Journal of Rare Earths

ELSEVIER

万方数据

Project for Enhancing International Impact of China STM Journals

CONTENTS

万方数据

JOURNAL OF RARE EARTHS
Vol. 37 No. 6 (June 2019)

CONTENTS

INVITED REVIEW

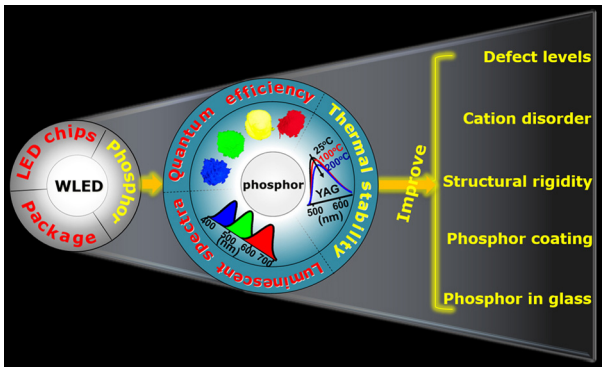

A significant challenge comes from the thermal quenching (TQ) behavior of the LED phosphors during the high-power operation or the updated laser lighting. This review proceeds from the mechanism of TQ, summarizes previous researches on the improving thermal stability of LED phosphors and discusses future research opportunities in this field

SPECTROSCOPY, LUMINESCENCE AND PHOSPHORS

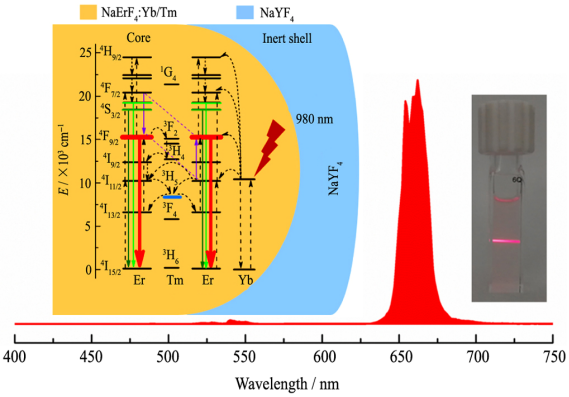

Both Yb doping and inert shell coating can greatly boost the single-band red upconversion luminescence in colloidal $NaErF_4$ nanocrystals

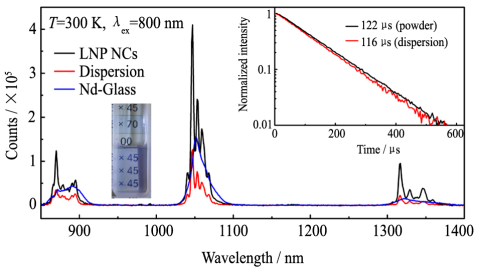

$LiNd(PO_3)_4$(LNP) nanocrystals, synthesized via improved combustion method, have strong emission intensity and a lifetime of 122 μs. Their dispersion in $DMSO/CHBr_2CHBr_2$ possess of high Nd^{3+} ions concentration (1×10^{20} cm^{-3}), long lifetime (116 μs), large emission cross section (7.63×10^{-20} cm^2) and high quantum yield (35.2%), would enable them to be the most potential gain medium of nanocrystals dispersion laser with LD pump

万方数据

RARE EARTH CATALYSIS

585 Synthesis of Cu/Ni-$La_{0.7}Sr_{0.3}Cr_{0.5}Mn_{0.5}O_{3-\delta}$ and its catalytic performance on dry methane reforming

Dingwen Kang, Jie Yu, Wenhui Ma, Min Zheng, Yunfei He, Pengfei Li

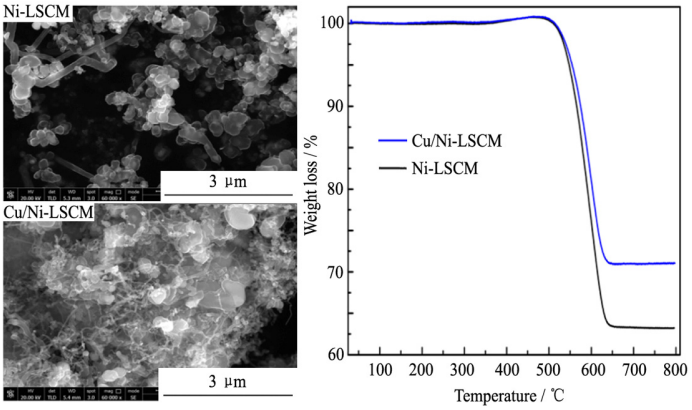

Active particles sizes and diameter of carbon filaments in Cu/Ni-LSCM are smaller than in Ni-LSCM after 13 h of dry methane reforming. The quantity of deposited carbon in Cu/Ni-LSCM is lower than in Ni-LSCM

J. Rare Earths, (37) 2019: 585-593

594 Effect of template on catalytic performance of $La_{0.7}Ce_{0.3}Ni_{0.7}Fe_{0.3}O_3$ for ethanol steam reforming reaction

Ping Yang, Ning Li, Junjiang Teng, Jian Wu, Hao Ma

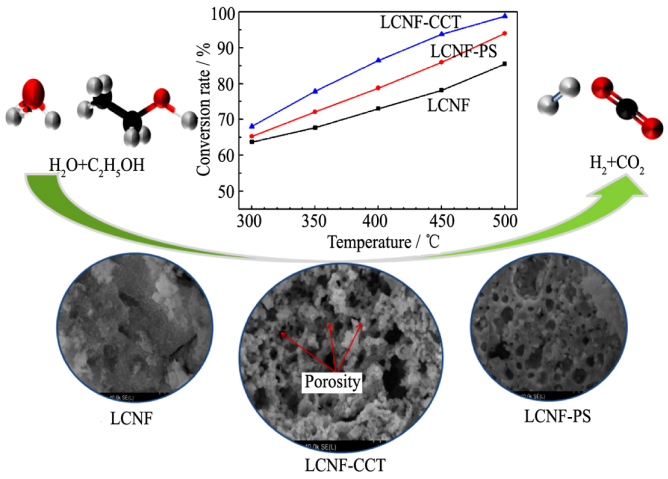

Perovskite-type oxides $La_{0.7}Ce_{0.3}Ni_{0.7}Fe_{0.3}O_3$ synthesized by using the polystyrene colloidal crystal templating (LCNF-CCT) possesses good redox properties, high specific surface area, regular pore size distribution and preferable oxygen species migration capability on the surface, presenting high catalytic activity for ethanol steam reforming reaction

J. Rare Earths, (37) 2019: 594-601

602 Lanthanum-doped Cu–Mn composite oxide catalysts for catalytic oxidation of toluene

Jing Pan, Wentao Du, Yongjun Liu, Yan Cheng, Shandong Yuan

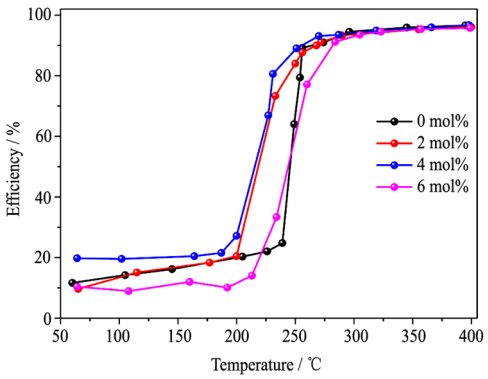

Catalytic performance of the catalysts (gas hourly space velocity: 30000 h^{-1}, toluene concentration: 1000 ppm) as a function of La loading. CuMn/La-2 mol% is observed to have a removal efficiency of 50% and 90% at 218 and 268 °C, respectively. CuMn/La-4 mol% exhibits the best activity, with 50% and 90% conversion at 217 °C (T_{50}) and 255 °C (T_{90}), respectively. Conversely, T_{50} and T_{90} for the La-free CuMn catalyst are as high as 245 and 274 °C, respectively. Further increasing the La doping level to 6 mol%, the activity performance is decreased, with T_{90} increasing to 280 °C. Results of the present work demonstrate that La-doping in Cu-Mn oxide catalysts can further enhance the catalytic performance toward toluene oxidation

J. Rare Earths, (37) 2019: 602-608

万方数据

609 Effects of precursor moisture and inert N_2 atmosphere calcinations on structure and properties of alumina modified CeZrLaNd mixed oxides

Meisheng Cui, Zhizhe Zhai, Hao Wang, Yongke Hou, Yongqi Zhang, Xiaowei Huang

J. Rare Earths, (37) 2019: 609-616

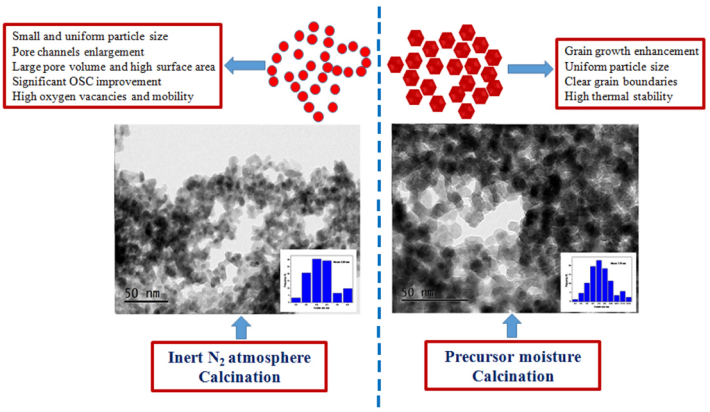

Precursor moisture and inert N_2 atmosphere calcinations both have great effects on the structure and properties of alumina modified CeZrLaNd mixed oxides

617 Synthesis, crystal structure and photocatalytic performance of polyoxometalate $K_{13}[Gd(GeW_{11}O_{39})_2]\cdot 34H_2O$

Haibin Liu, Lin Bai, Limei Ai, Wenshuang Dai, Danfeng Zhang, Qingyin Wu, Renchun Zhang

J. Rare Earths, (37) 2019: 617-621

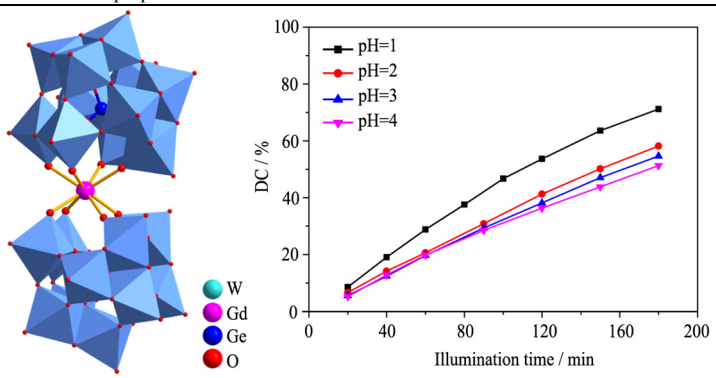

A polyoxometalate $K_{13}[Gd(GeW_{11}O_{39})_2]\cdot 34H_2O$ was synthesized and characterized. The heteropolyanion of $[Gd(GeW_{11}O_{39})_2]^{13-}$ consists of two $[GeW_{11}O_{39}]^{8-}$ vacant Keggin moieties linked via Gd^{3+}. Photocatalytic performance of $K_{13}[Gd(GeW_{11}O_{39})_2]\cdot 34H_2O$ in photodegradation of X-3B was also studied. When the reaction time is 180 min, the decoloring rate reaches 71.19%. With the decrease of pH, the decolorization rate increases gradually

MAGNETISM AND MAGNETIC MATERIALS

622 Magnetic properties and magnetic entropy change of perovskite manganites $La_{0.9-x}Eu_xSr_{0.1}MnO_3$ (x=0.000, 0.075) by experimental method and numerical fitting

Xiang Jin, Jianjun Zhao, Hongye Wu, Bao Xu, Yunbin Sun, Xiaodong Sun, Fengze Cao, Kai Wang, Wenxing Wang, Yutong Zhang, Yi Lu

J. Rare Earths, (37) 2019: 622-627

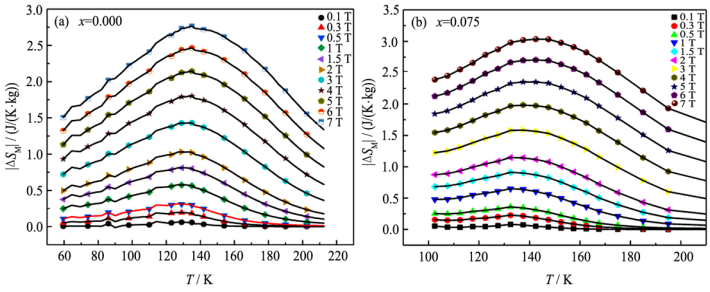

The maximum magnetic entropy change $|\Delta S_M|$ value of the samples $La_{0.9-x}Eu_xSr_{0.1}MnO_3$ (x=0.000, 0.075) near the Curie temperature (T_C) reaches 2.76 and 3.03 J/(K·kg), respectively. In addition, the relative cooling power (RCP) is found to be 425.28 and 443.53 J/kg. Both samples have the potential to realize magnetic refrigeration in the high temperature region (T>77 K)

628 Micromagnetic simulations on demagnetization processes in anisotropic $Nd_2Fe_{14}B$ magnets

Lei Li, Shengzhi Dong, Rui Han, Kuikui Song, Dong Li, Minggang Zhu, Wei Li, Wei Sun

J. Rare Earths, (37) 2019: 628-632

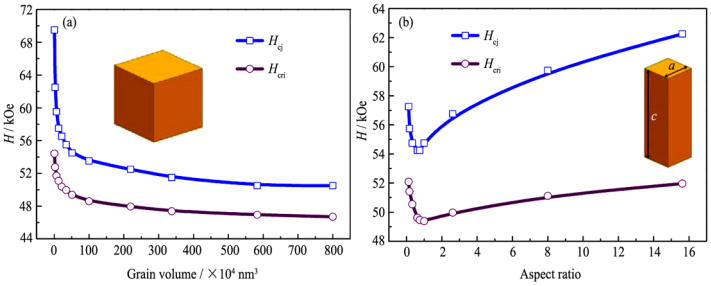

As for cubic grains, the coercive field presents descending tendency as grain volume ascends. Under constant grain volume, with aspect ratio increasing, the coercive field decreases in the beginning and increases soon. Based on the demagnetization field vector, the calculated critical field always shows the same tendency as the coercive field for all cases of this study. It can be concluded that critical field is qualified to be a reference index to measure the magnitude of coercive field

万方数据

633 Corrosion behavior and magnetocaloric effect of FeNi (1J85) coated $LaFe_{11.6}Si_{1.4}$/Sn composites

Xi Zhao, Ping Fang, Yongbai Tang, Yungui Chen, Lingtong Zhou, Huaqiang Guo

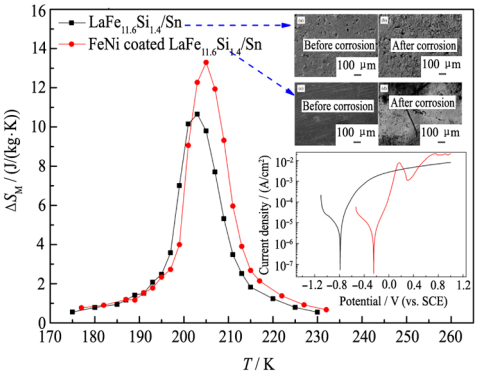

FeNi coating can improve the magnetocaloric effect and the corrosion resistance of the composite magnetic refrigerant ($LaFe_{11.6}Si_{1.4}$/Sn composites), including the values of RCP and $(-\Delta S_M)^{max}$, and the corrosion potential

J. Rare Earths, (37) 2019: 633-637

638 Corrosion mechanism of H_2O on Sm_2Fe_{17} and nitrogenation process of corroded Sm_2Fe_{17}

Jianwei Xu, Jingwu Zheng, Haibo Chen, Liang Qiao, Yao Ying, Wei Cai, Wangchang Li, Jing Yu, Min Lin, Shenglei Che

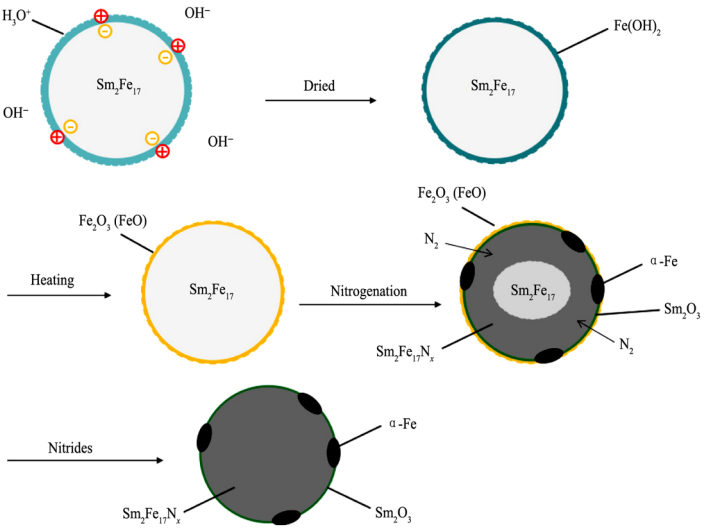

Metallic hydroxide forms and deposits on the Sm_2Fe_{17} powder surfaces during water corrosion. In the subsequent nitrogenation process, the hydroxide dehydrates and hydrogen are desorbed. The generated oxide reacts with $Sm_2Fe_{17}N_x$, forming α-Fe and Sm_2O_3

J. Rare Earths, (37) 2019: 638-644

ADVANCED RARE EARTH MATERIALS

645 Grain boundary segregation and its influences on ionic conduction properties of scandia doped zirconia electrolytes

Qiannan Xue, Xiaowei Huang, Jianxing Zhang, He Zhang, Zongyu Feng

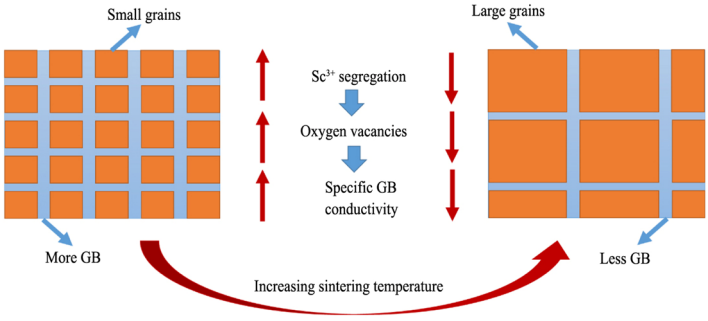

The bulk and grain boundary ionic conductivity of 1Ce10ScSZ system increases with the increasing grain size. However, the specific grain boundary conductivity decreases with the increasing grain size. This is explained by the fact that Sc^{3+} is segregated at the grain boundary, which leads to higher oxygen vacancy concentration when sintered at lower temperature

J. Rare Earths, (37) 2019: 645-651

万方数据

CHEMISTRY AND HYDROMETALLURGY

652 Simultaneous recovery of rare earth elements and phosphorus from phosphate rock by phosphoric acid leaching and selective precipitation: Towards green process

Shengxi Wu, Longsheng Zhao, Liangshi Wang, Xiaowei Huang, Yunhan Zhang, Zongyu Feng, Dali Cui

J. Rare Earths, (37) 2019: 652-658

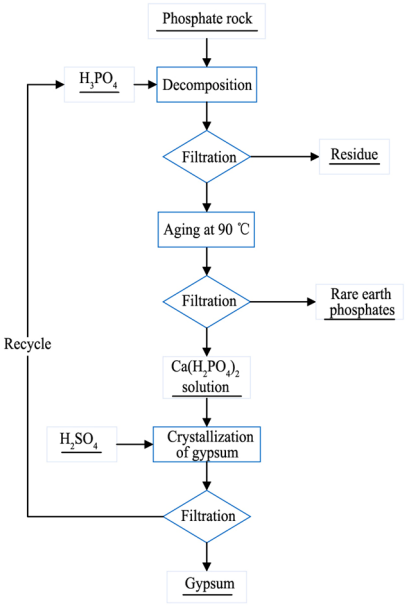

A green recycle flow-sheet for simultaneous recovery of REEs and phosphorus from phosphate rock

METALLOGRAPHY AND PYROMETALLURGY

659 Microstructure and mechanical properties of A356 alloy with yttrium addition processed by hot extrusion

Zhifan Wei, Yushun Lei, Hong Yan, Xihao Xu, Jiajia He

J. Rare Earths, (37) 2019: 659-667

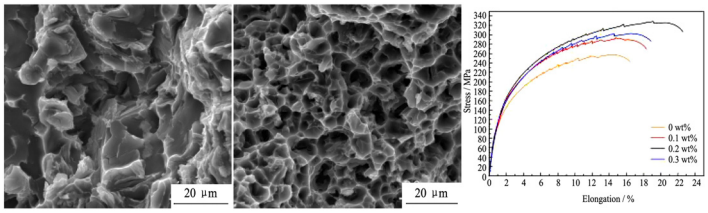

The microstructures, the mechanical properties and the fracture surfaces of A356 alloy were investigated. Under extruding stress, the fracture morphology of the as-extruded A356 alloy with 0.2 wt% Y is changed. The cleavage platforms disappear and are completely transformed into dimples. The dimples are small in size, regular in shape, and uniformly distributed, which are characteristics of a typical dimple fracture. Compared with the as-cast alloys, the plasticity of the as-extruded alloys has been greatly enhanced. When 0.2 wt% Y is used, the ultimate tensile strength, and elongation of the alloy reach the maximum, which are 328.2 MPa and 21.3%, respectively and increase by 42.01% and 481.91%, respectively, in comparison to the as-cast alloy without the addition of Y

668 Double-shell structure of $Al_3(Zr,Sc)$ precipitate induced by thermomechanical treatment of Al–Zr–Sc alloy cable

Jiayi Zhang, Tao Hu, Danqing Yi, Hongxuan Wang, Bin Wang

J. Rare Earths, (37) 2019: 668-672

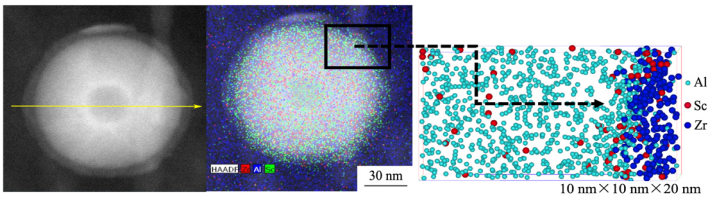

A spheroidal $Al_3(Zr,Sc)$ precipitate with a double-shell structure after thermomechanical treatment. This double-shell structure comprises a Sc-enriched core enveloped by a Zr-enriched inner shell and a Sc-enriched outer shell. The double-shelled $Al_3(Zr,Sc)$ precipitate presents three different interfaces and is semicoherent with the Al matrix. Three dimensional atom-probe shows the outer shell of $Al_3(Zr,Sc)$ precipitate is Sc element enrichment

RARE EARTH APPLICATIONS

673 Elevated temperature wear behaviour of CeO_2 modified WC-12Co coating

Yan Liu, Guiying Yang, Zongqiu Hang, Hao Fu, Naiyuan Xi, Hui Chen

J. Rare Earths, (37) 2019: 673-678

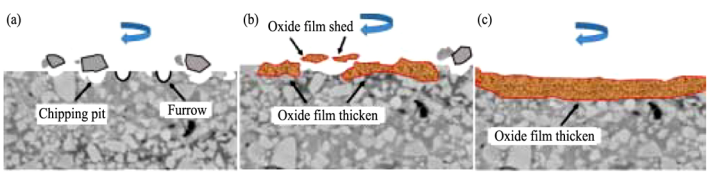

Micro cutting wear, abrasive wear and oxidation wear dominate the wear mechanism at 450 ℃ (a), 550 ℃ (b) and 650 ℃ (c), respectively

万方数据